J Adv Ceram

Research Article

Bioinspired Bouligand structure for the synergistic enhancement of mechanical and thermal properties in 3D-printed C_{sf}/ZrB_2-SiC composites

Yang Hu[2,3,4], Jun Lu[2,3], Dewei Ni[1,2,3,✉], Bowen Chen[2,3], Feiyan Cai[2,3], Yanmei Kan[2,3], Yusheng Ding[2,3], Shaoming Dong[2,3]

Cite this article: Hu Y, Lu J, Ni D, et al. *J Adv Ceram* 2026, **15**(2): 9221232. https://doi.org/10.26599/JAC.2025.9221232

ABSTRACT: Short carbon fiber reinforced ultrahigh temperature ceramic matrix composites (C_{sf}/UHTCMCs) are recognized as leading candidates for thermal structures owing to their precisely tailorable composition and enhanced tunability in structure and properties. Inspired by nature, the Bouligand structure—characterized by a gradual angular rotation between successive layers—exhibits remarkable load-bearing and thermal conductive capacity. In this study, the Bouligand structure was introduced into C_{sf}/ZrB_2-SiC by employing direct ink writing technology. The results indicate that the composite with a 30° interlayer Bouligand structure achieves a synergistic improvement in both mechanical performance and thermal diffusion uniformity. Specifically, enhancements of 42% in flexural strength and 35% in fracture toughness were achieved compared to conventional C_{sf}/ZrB_2-SiC. Meanwhile, the *Z*-axis thermal conductivity increased by 24.5%, along with a notable enhancement of in-plane thermal diffusion. These improvements can be attributed to the smaller deflection angles and more frequent unidirectional deflections within the 30° Bouligand structure, which promote more pronounced crack deflection. Furthermore, the small-angle rotational design improves in-plane thermal diffusion uniformity by leveraging the high intrinsic radial thermal conductivity of short carbon fibers. Hence, the bioinspired Bouligand structure design offers a promising strategy for the synergistic optimization of mechanical and thermal properties in C_{sf}/UHTCMCs.

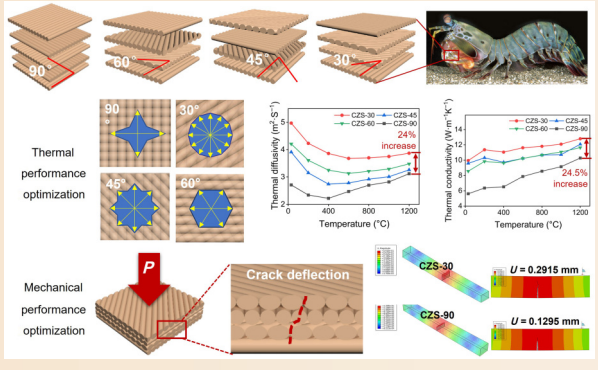

KEYWORDS: bioinspired Bouligand structure; short fiber-reinforced ceramic matrix composites; 3D printing; structure optimization; mechanical and thermal properties

1 Introduction

The rapid development of aerospace and hypersonic vehicle technology places stringent performance demands on thermal structural materials [1–4]. Thermal structural materials must maintain stable mechanical properties and chemical inertness in extreme environments exceeding 2000 °C while also possessing excellent thermal shock resistance [5–9]. Fiber-reinforced ultrahigh-temperature ceramic matrix composites (UHTCMCs) effectively overcome the intrinsic brittleness of monolithic ceramics, combining advantages such as low density, ultrahigh temperature stability and excellent ablation resistance [10–12]. As a result, UHTCMCs are regarded as a leading candidate for thermal structures in extreme environments of the above applications [13].

Particle-reinforced ceramics rely on the introduction of higher modulus particles to facilitate crack deflection. However, the toughening effect in particle-reinforced ceramics is limited; the fracture behavior of the material remains inherently brittle. In contrast, short fiber reinforced ceramic matrix composites (C_{sf}/UHTCMCs) have a suite of active toughening mechanisms. Fiber bridging enables the material to continue bearing load even after the matrix has cracked. Fiber pull-out is a key mechanism that dissipates energy through extensive frictional work. The synergistic effect between these two mechanisms enables a transition in short fiber-reinforced composites from brittle to

[1] Hangzhou Institute for Advanced Study, University of Chinese Academy of Sciences, Hangzhou 310024, China. [2] State Key Laboratory of High Performance Ceramics, Shanghai Institute of Ceramics, Chinese Academy of Sciences, Shanghai 200050, China. [3] Structural Ceramics and Composites Engineering Research Center, Shanghai Institute of Ceramics, Chinese Academy of Sciences, Shanghai 200050, China. [4] University of Chinese Academy of Sciences, Beijing 100049, China.

✉ Corresponding author. E-mail: deweini@mail.sic.ac.cn

Received: October 13, 2025; Revised: November 28, 2025; Accepted: December 17, 2025

nonbrittle fracture behavior. C_{sf}/UHTCMCs exhibit high fracture toughness and superior damage tolerance [14–17]. This makes C_{sf}/UHTCMCs highly promising for thermal protection systems in advanced vehicles. However, conventional processing routes for C_{sf}/UHTCMCs often cause severe mechanical degradation and chemical damage to the fibers, and the random fiber distribution makes precise microstructural control extremely challenging [17–19]. The recent development of additive manufacturing (3D printing), particularly direct ink writing (DIW), has revolutionized the fabrication of advanced ceramics by enabling complex geometries and tailored microstructures [11,20,21]. This technique allows precise control over the printing path to achieve oriented fiber alignment in three-dimensional space.

Nevertheless, C_{sf}/UHTCMCs fabricated via traditional 3D printing with 90° interlayer angles contain structurally weak zones, which impede the controlled design of crack propagation paths and limit effective toughening [22]. A notable example of a superior natural architecture is the Bouligand structure, which consists of helically stacked nanofiber lamellae [21,23]. Biological tissues such as the hammer of the stomatopod, fish scales, and lobster underbelly exhibit Bouligand structural characteristics, resulting in remarkable mechanical properties [24–27]. The defining feature of the Bouligand structure is its helical stacking of multiple layers, where fibers are aligned within each layer but exhibit a consistent misorientation angle between adjacent layers [28–30]. This sophisticated architecture promotes crack deflection and extension under mechanical loading, effectively dissipating fracture energy and achieving a synergistic combination of high strength and toughness [31]. Introducing the bioinspired Bouligand structure design into C_{sf}/UHTCMCs offers a novel strategy for enhancing mechanical properties.

In this study, C_{sf}/ZrB_2-SiC Bouligand structure composites with varying pitch angles were designed and fabricated using DIW. Finite element simulations of crack propagation paths were first conducted for an initial mechanical assessment of the samples with varying pitch angles. Experimental evaluations of bending strength and fracture toughness revealed that the Bouligand structure with a 30° interlayer angle exhibited the highest mechanical performance. Additionally, the 30° Bouligand structure enhanced the thermal conductivity along the *Z*-axis and improved the in-plane thermal uniformity. This characteristic is pivotal for reducing the surface response temperature and extending the service lifetime in extreme high-temperature environments. This work demonstrates the successful application of a bioinspired Bouligand structure in UHTCMCs. This study offers a new strategy for the development of advanced thermal structural materials.

2 Experimental

2.1 Raw materials

Commercially available ZrB_2 (purity > 99%, particle size: 0.1–1 μm (Fig. S1 in the Electronic Supplementary Material (ESM)); Shanghai Yaotian New Material Technology, China) and short carbon fibers (M40, average length: 100–500 μm (Fig. S1 in the ESM); Toray Industries, Japan) were used as the raw materials. Polyvinyl butyral (PVB, M_w = 90,000–120,000, purity: 99%; Aladdin, China) was used as a dispersing agent.

2.2 Fabrication of C_{sf}/ZrB_2-SiC Bouligand structure composites

C_{sf} and PVB (constant weight ratio of PVB : C_{sf} = 1 : 3) were first added to deionized water to prepare a uniformly dispersed fiber suspension by ultrasonication. ZrB_2 powder was added to the above solution with continued stirring in a water bath at 60 °C. C_{sf}/ZrB_2 paste was obtained after deionized water evaporation, and the suspension became toothpaste-like. After that, C_{sf}/ZrB_2 paste was transferred into a print nozzle and installed in a DIW printer (3D bioprinter V2.0, Regenovo Biotechnology Co., Ltd., China). C_{sf}/ZrB_2 preforms were printed using a nozzle with an inner diameter of 0.84 mm driven by nitrogen at a pressure of 0–0.6 MPa. The speed of the nozzle moving in the *x*-axis and *y*-axis directions was set to 0–5 mm·s^{-1}, and the distance between filaments was set to 0.5 mm. The C_{sf}/ZrB_2 preforms were printed layer by layer, with successive layer rotations of 30°, 45°, 60°, and 90°. The composites with interlayer angles of 30°, 45°, 60°, and 90° were referred to as CZS-30, CZS-45, CZS-60, and CZS-90, respectively. Schematic diagrams for all the samples are shown in Fig. 1. The printed C_{sf}/ZrB_2 performs were dried at 55 °C for 24 h. After that, polycarbosilane (PCS; National University of Defense Technology, China) was used to further densify the C_{sf}/ZrB_2 preforms and pyrolyzed at 1100 °C in an Ar atmosphere. The precursor infiltration and pyrolysis (PIP) process of PCS was repeated six times.

2.3 Characterizations

The microstructure of the composites was characterized using a field emission scanning electron microscope (FESEM; Hitachi SU8220, Japan). Phase composition was analyzed by an X-ray diffractometer (XRD; D8 Discover Davanci, Bruker Co., Germany). The flexural strength of the composites was evaluated by a three-point bending test (60 mm × 6 mm × 4 mm test bars) with a span of 50 mm and a loading rate of 0.5 mm·min^{-1}. The fracture behavior of the composites was measured by a single-edge-notched beam (SENB) method with a specimen size of 30 mm × 6 mm × 3 mm, notch length of 3 mm, notch depth of 1.5 mm, crosshead speed of 0.5 mm/min, and support span of 24 mm. Thermal diffusivity was measured by a laser flash thermal conductivity meter (LFA467 HT, NETZSCH, Germany). The sample size used for thermal diffusivity measurement is Φ10 mm × 2 mm. Thermal conductivity was calculated according to Eq. (1):

$$\lambda = \alpha C_p \rho \tag{1}$$

where λ and α are the thermal conductivity (W·m^{-1}·K^{-1}) and the thermal diffusivity (m^2·s^{-1}), respectively, and C_p and ρ are the specific heat (J·g^{-1}·K^{-1}) and the density (kg·m^{-3}) of the composites, respectively.

3 Results and discussion

3.1 Microstructure and phase composition of as-fabricated C_{sf}/ZrB_2-SiC composites

The phase composition of the as-fabricated composites was characterized by XRD. No additional impurities were discernible beyond the characteristic peaks of ZrB_2 and graphitic carbon (Fig. 2(a)). Interestingly, the signal of CZS-90 was relatively low. For the same crystalline phase, the positions of the diffraction peaks in the XRD patterns remain consistent, while their intensities may vary, which is a common occurrence in XRD analysis. A possible explanation involves the samples being analyzed in different batches, combined with a potentially high scan speed during the CZS-90 measurement, resulting in lower peak intensities. The results may be influenced by the instrument's condition and specific parameters during testing. This does not

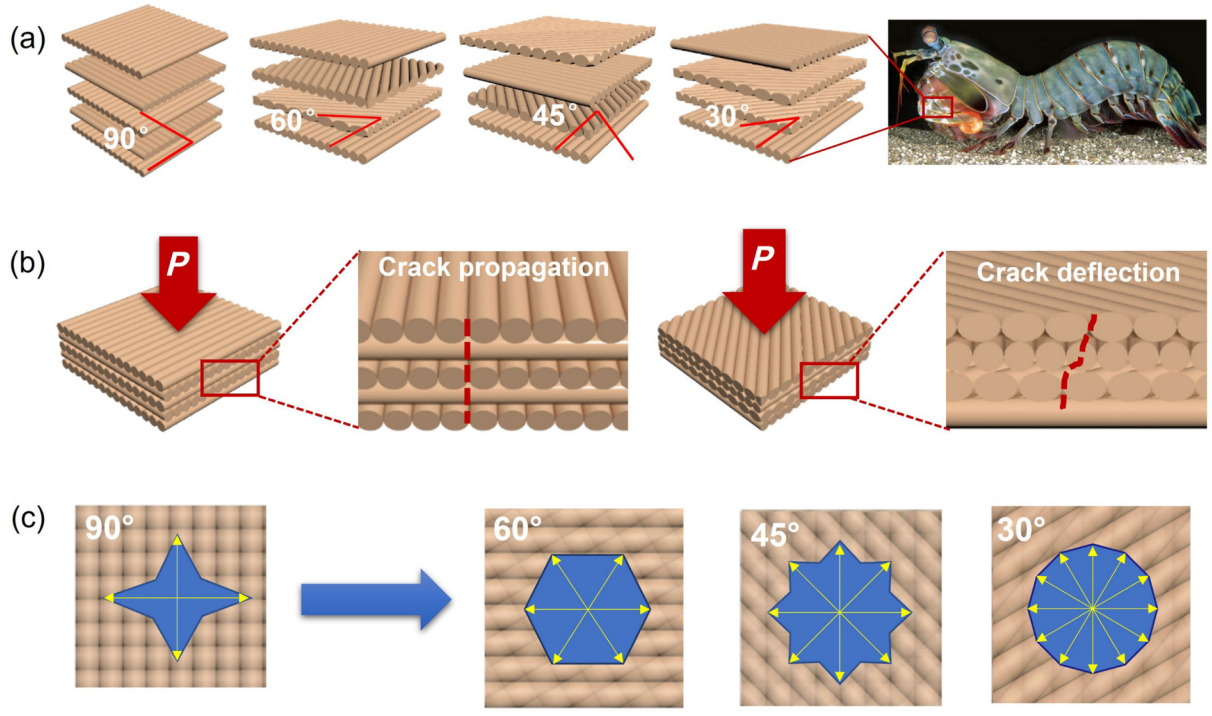

Fig. 1 (a) Schematic diagrams of the four C_{sf}/ZrB_2-SiC composites fabricated in this work; (b) Schematics of crack deflection in the presence and absence of Bouligand structure in the C_{sf}/ZrB_2-SiC composites; (c) schematics of in-plane thermal diffusion in the C_{sf}/ZrB_2-SiC composites.

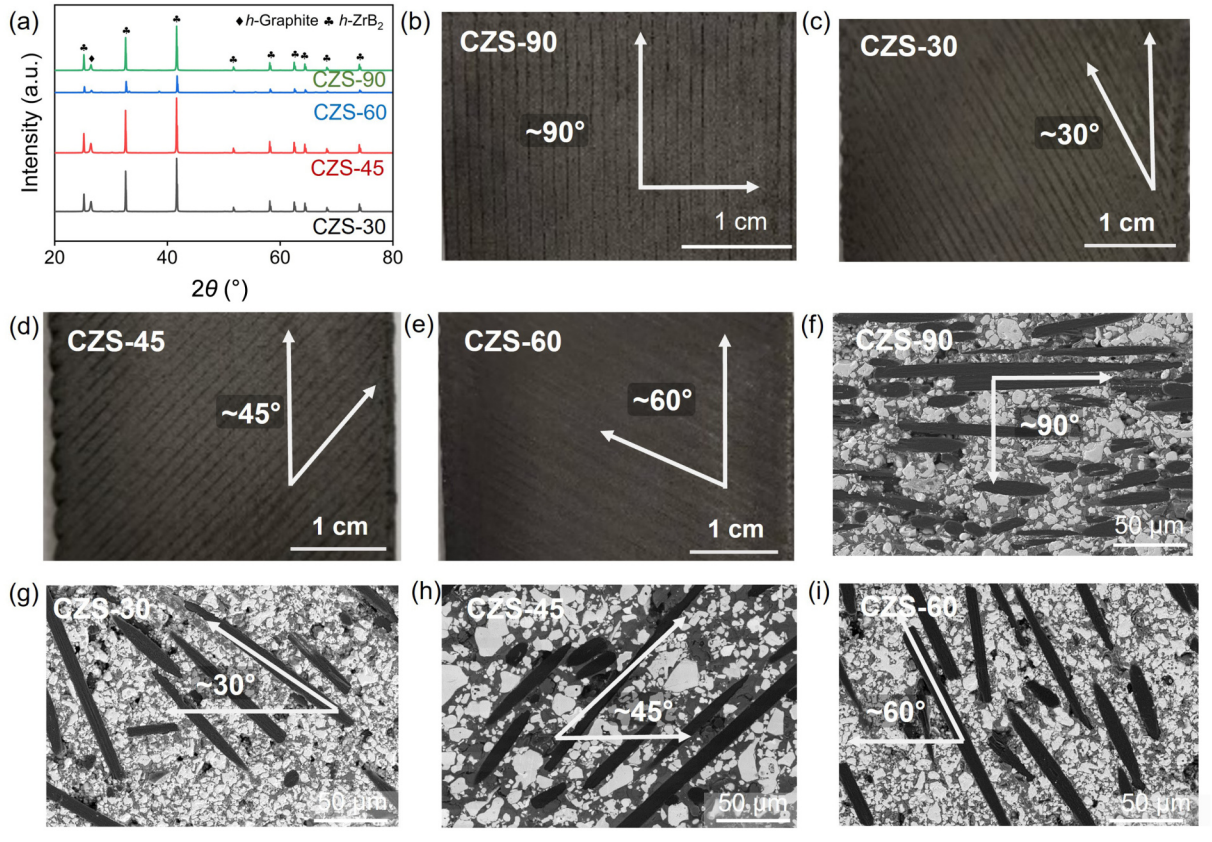

Fig. 2 (a) XRD patterns of the as-fabricated C_{sf}/ZrB_2-SiC composites; (b–e) macroscopic surface morphology characteristics of CZS-90, CZS-30, CZS-45, and CZS-60; (f–i) microscopic cross-sectional morphology characteristics of CZS-90, CZS-30, CZS-45, and CZS-60.

affect the phase identification. These results confirm the high purity of the as-fabricated sample, indicating its suitability for investigating the mechanical and thermal properties. The SiC phase is identified as amorphous. SiC was introduced via PIP. The PIP process was carried out at approximately 1100 °C. This pyrolysis temperature results in the formation of an amorphous SiC phase. This phenomenon is consistent with observations reported in previous studies [32].

Figures 2(b) and 2(f) show the macroscopic and microstructure of the C_{sf}/ZrB_2-SiC composite fabricated by 3D printing with a 90° interlayer angle. Apart from porosity originating from the PIP process, the chopped fibers were all aligned in a parallel direction (0°). The porosity of CZS-90 was determined to be 15.78% by the Archimedes method, which quantifies the composites' open porosity. Based on the characteristics of the fabrication process, it is reasonable to attribute the composites' porosity primarily to the inherent 3D printed structure and the shrinkage occurring during the PIP process. The 3D printing process introduces macroscopic pores with dimensions on the order of tens to hundreds of micrometers. The composite was subsequently densified via the PIP process. Not all pores are filled during the PIP process, leading to the formation of residual porosity within the composite. Such pores typically range from the submicrometer scale to the nanoscale and are randomly distributed within the composites. A comparative analysis of the macroscopic (Figs. 2(c)–2(e)) and microscopic (Figs. 2(g)–2(i)) images of the C_{sf}/ZrB_2-SiC composites with the Bouligand structure clearly reveals their distinct structural characteristics at various angles. The alignment angles of the chopped fibers closely matched the sets. These characterizations directly confirm the successful fabrication of all designed C_{sf}/ZrB_2-SiC composites with distinct angles. The fiber orientation degrees for the CZS-30, CZS-45, and CZS-60 composites were determined to be 0.81, 0.83, and 0.79, respectively. All the samples exhibited a uniform distribution of the fibers and the matrix. Identical slurry compositions and 3D printing parameters (except for the deflection angle) were used for all four samples, resulting in comparable fiber contents across the samples.

3.2 Mechanical behavior and mechanisms of the C_{sf}/ZrB_2-SiC composites with a Bouligand structure

In this study, finite element analysis (FEA) was first employed to simulate the crack propagation paths during three-point bending tests in the four C_{sf}/ZrB_2-SiC composites fabricated in this work. To simplify the modeling and computation, the tows were modeled as aligned fiber bundles. The fiber tow diameter was set to 0.6 mm, which is close to the value observed in the composites. Furthermore, the model was set up with the ZrB_2-SiC matrix occupying the interbundle regions. The model dimensions were set to 60 mm × 6 mm × 4 mm. The model dimensions were defined in accordance with the standard requirements for three-point bending testing. Composites with distinct structures were fabricated by rotating each successive layer by 30°, 45°, 60°, and 90° relative to a 0° initial layer. The models of CZS-30, CZS-45, CZS-60, and CZS-90 are depicted in Fig. 3(a). The green and gray areas in the model denote the fiber and the ZrB_2-SiC matrix, respectively. The central dark blue or dark red region was set as the loading area.

The computational parameters were set to a load range of 0–10 kN and a loading rate of 0.5 mm·s^{-1}. A 1.5-mm-deep notch was preconfigured at the sample center. In accordance with the fracture toughness testing standard, a notch was introduced at the center of the specimen, which featured a rectangular tip. In the simulations, failure was defined as the attainment of a critical displacement (U), with both the failure displacement and crack propagation path recorded upon fracture. As illustrated in Fig. 3(b), the simulated failure displacements and crack paths revealed distinct behaviors across samples:

CZS-90: The crack propagated along an almost linear trajectory, fracturing at a displacement of 0.1295 mm, indicating inferior mechanical performance.

CZS-45: Despite slight crack deflection, fracture occurred at a displacement of 0.1919 mm, suggesting mechanical properties comparable to CZS-90.

CZS-60: Significant crack deflection and a larger central displacement were observed, demonstrating superior mechanical properties to CZS-45.

CZS-30: This sample exhibited the largest failure displacement (0.2915 mm) and multiple crack deflections, confirming its optimal mechanical performance among all tested configurations.

The FEA results conclusively demonstrate that the Bouligand structure with a 30° interlayer angle exhibits the highest mechanical performance, highlighting the critical role of tailored interlayer angles in enhancing composite properties.

To validate the accuracy of the simulated results, mechanical property tests were performed on all four fabricated samples. To meet the standard thickness requirements of the test, the number of layers was set at six for mechanical testing. The experimental data demonstrated a clear performance hierarchy: while ZS-45

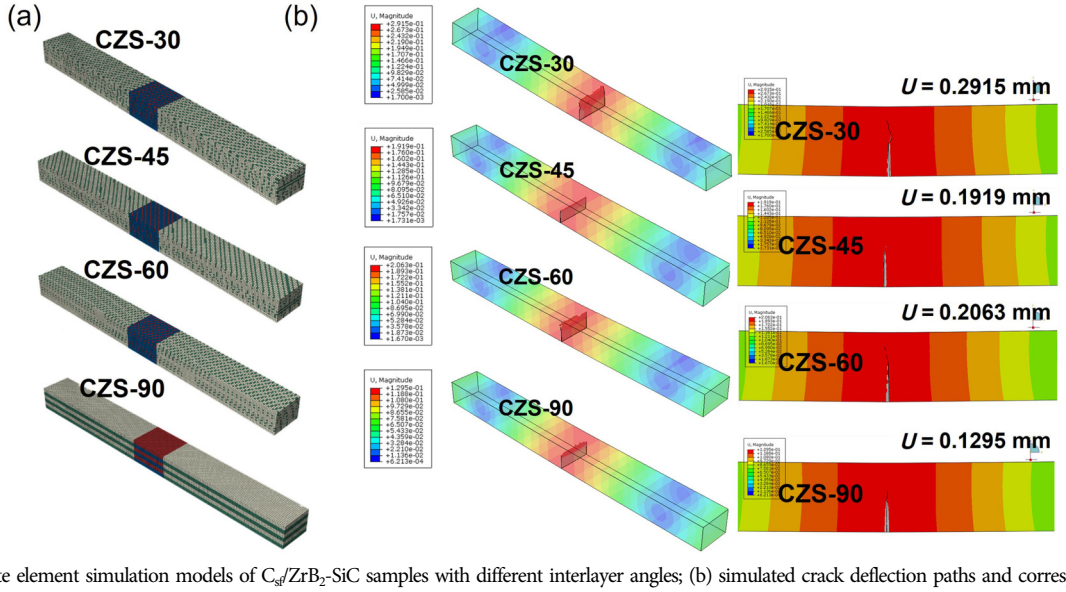

Fig. 3 (a) Finite element simulation models of C_{sf}/ZrB_2-SiC samples with different interlayer angles; (b) simulated crack deflection paths and corresponding critical failure displacement of the samples.

exhibited the lowest mechanical properties, the CZS-30 sample achieved the highest performance metrics, with the CZS-60 sample showing intermediate characteristics (Fig. 4(a)). This close alignment between the experimental and simulation outcomes confirms the reliability of the computational model. Remarkably, the CZS-30 sample outperformed the others in three key mechanical parameters: flexural strength (increased by ~42%), fracture toughness (enhanced by 35%), and fracture work (improved by 72%) compared to the CZS-90 baseline (Figs. 4(b)–4(d)). Furthermore, the mechanical strength of the composite prepared in this work (64.7 MPa) significantly surpasses that of a previously reported Bouligand structure composite (36.9 MPa) [22]. These findings underscore the pivotal role of the small-angle (30°) Bouligand structure in optimizing mechanical performance through tailored architectural design. The simulation results show that CZS-30 exhibits the largest critical displacement, indicating its superior mechanical performance. The superior flexural strength of CZS-30 was determined experimentally by three-point bending tests. The experimental data and the simulation data are not directly comparable. This work identifies the optimal Bouligand structure for mechanical performance through a combined experimental and simulation approach.

To elucidate the mechanism underlying the enhanced mechanical performance, fracture morphology characterization was conducted. Fig. 5 presents the crack propagation paths and corresponding fracture surfaces of all four samples. The CZS-90

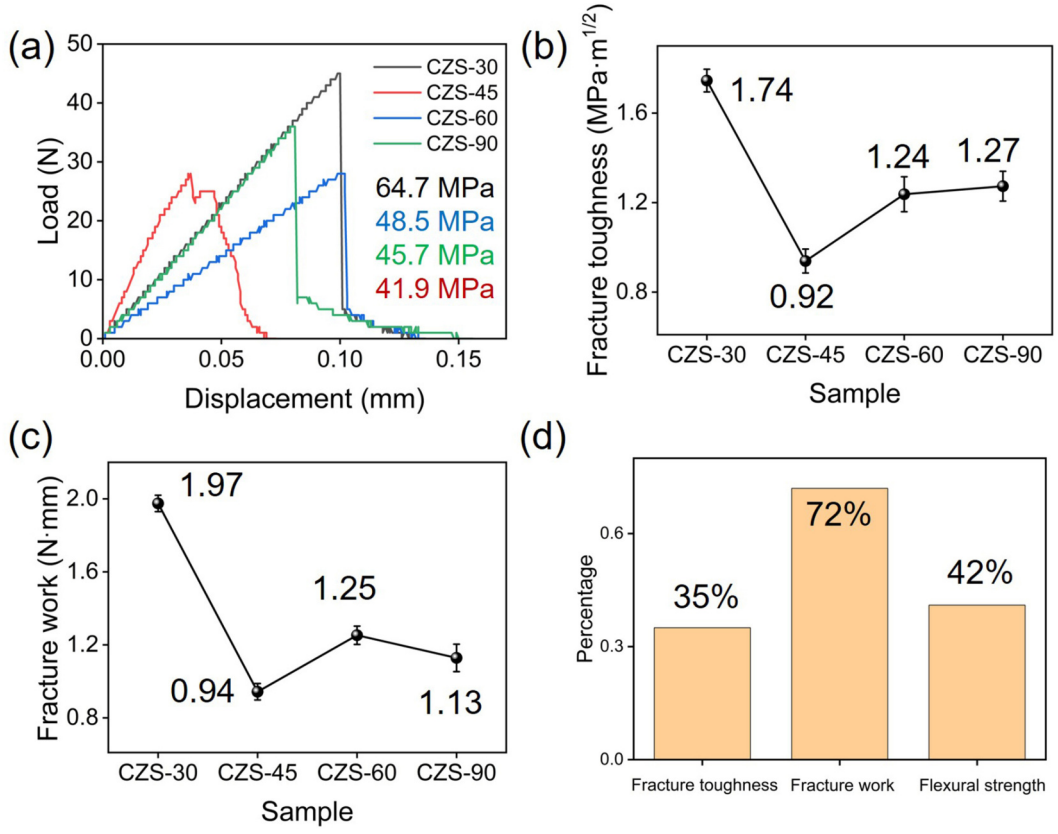

Fig. 4 (a) Load–displacement curves of the C_{sf}/ZrB_2-SiC samples during bending tests; (b, c) fracture toughness and fracture work of the samples; (d) percentage increase in fracture toughness, flexural strength, and fracture work of CZS-30 compared to CZS-90.

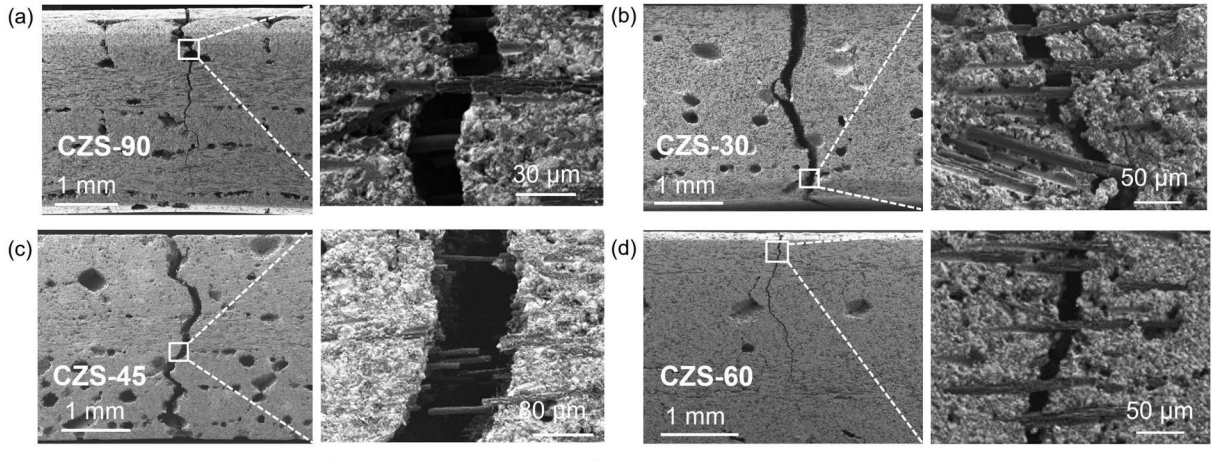

Fig. 5 Cross-sectional fracture morphologies of the C_{sf}/ZrB_2-SiC samples with different interlayer angles at low and high magnifications: (a) CZS-90 sample; (b) CZS-30 sample; (c) CZS-45 sample; (d) CZS-60 sample.

清華大学出版社 Tsinghua University Press | SciOpen

sample displayed a smooth macrofractured surface with an almost linear crack path (Fig. 5(a)), a finding consistent with the simulation results. In contrast, composites with Bouligand structures exhibited nonlinear crack propagation, demonstrating the structural role of interlayer angles in fracture resistance. Key functional differences were observed among fiber layers. For the 0° layers, fibers oriented perpendicular to the crack direction impeded propagation through energy dissipation via fiber pull-out. The intermediate-angle layers (e.g., 30°–60°) provided graded resistance by deflecting cracks through helical interfaces. For the 90° layers, fibers aligned parallel to the crack path offered minimal resistance, relying solely on weak interfacial bonding for retardation. This hierarchical fiber alignment explains both the linear crack trajectory and inferior mechanical performance of CZS-90, whereas Bouligand-structured samples (particularly CZS-30) achieved superior performance through multiscale crack deflection.

In Bouligand-structured composites, layers with intermediate angles (termed "twisted layers") between 0° and 90° play a pivotal role in mechanical enhancement through crack-twisting mechanisms. The interlayer rotation angles promote crack deflection along helical interfaces, while the fiber alignment within each layer guides crack propagation and impedes its advancement via energy dissipation.

The influence of the Bouligand structure on the mechanical properties was analyzed by examining the crack propagation path in the fracture surface of CZS-30. The crack path exhibited alternating left-right deflections (Fig. 5(b)), with small-angle fibers (30° to *X*-axis) demonstrating pronounced fiber bridging and pull-out effects. Frequent deflections in consistent directions and full activation of energy dissipation mechanisms (e.g., interfacial debonding) contributed to its optimal mechanical performance. Limited crack deflection (Fig. 5(c)) resulted in reduced energy absorption, as only partial fiber pull-out occurred in intermediate-angle layers. The lower fracture toughness compared to CZS-30 aligns with reported trends where 40°–45° Bouligand angles show suboptimal crack-twisting efficiency. Although crack deflection initiated leftward before backward shifting (Fig. 5(d)), the large fiber angles (> 60°) in deflection layers diminished toughening effects such as fiber pull-out. The absence of 90° layers forced crack deflection at every interface, explaining its superior performance compared to CZS-45 despite less pronounced deflections. CZS-30's superiority stems from its smaller deflection angles (enhancing fiber-matrix interfacial interactions) and higher deflection frequency, which maximize energy dissipation through multiscale crack twisting and bridging, a phenomenon consistent with natural Bouligand structures. To facilitate statistical analysis, the SEM image of the fracture surface in Fig. 5 has been magnified and optimized. It can be observed that a greater number of fibers in the Bouligand structure composite participate in impeding crack propagation. The fiber pull-out length in CZS-45 is significantly greater than that in CZS-90. Furthermore, the Bouligand structure composite exhibits a markedly higher degree of crack deflection than CZS-90. However, the variation in fiber pull-out length at different fracture sites prevents a conclusive interpretation of the crack deflection and energy dissipation mechanisms based solely on local SEM analysis.

3.3 Effect of the Bouligand structure on thermal properties and mechanisms

To elucidate the role of the Bouligand structure in thermal transport anisotropy, we systematically characterized the thermal conductivity (λ) and diffusivity (α) of four samples along both the *Z*-axis and in-plane directions (Fig. 6(a)). To meet the standard thickness requirements of the test, the number of layers was set at three for thermal testing. Despite comparable compositional profiles and nondirectional fiber distribution along the *Z*-axis, both λ and α increased monotonically with decreasing interlayer angle (Figs. 6(b) and 6(c)). Specifically, the CZS-30 sample demonstrated superior *Z*-axis thermal performance, achieving enhancements of approximately 24.5% in thermal conductivity and 24% in thermal diffusivity at 1200 °C compared to CZS-90. The three schematic diagrams in Figs. 6(d)–6(f) depict the cross-section of three distinct Bouligand structure composites. All three models are oriented in the *X*–*Z* plane. The three porosity values in the models of Figs. 6(d)–6(f) correspond to the overall porosity of the three respective Bouligand structure composites. The porosities of CZS-30, CZS-45, CZS-60, and CZS-90 were

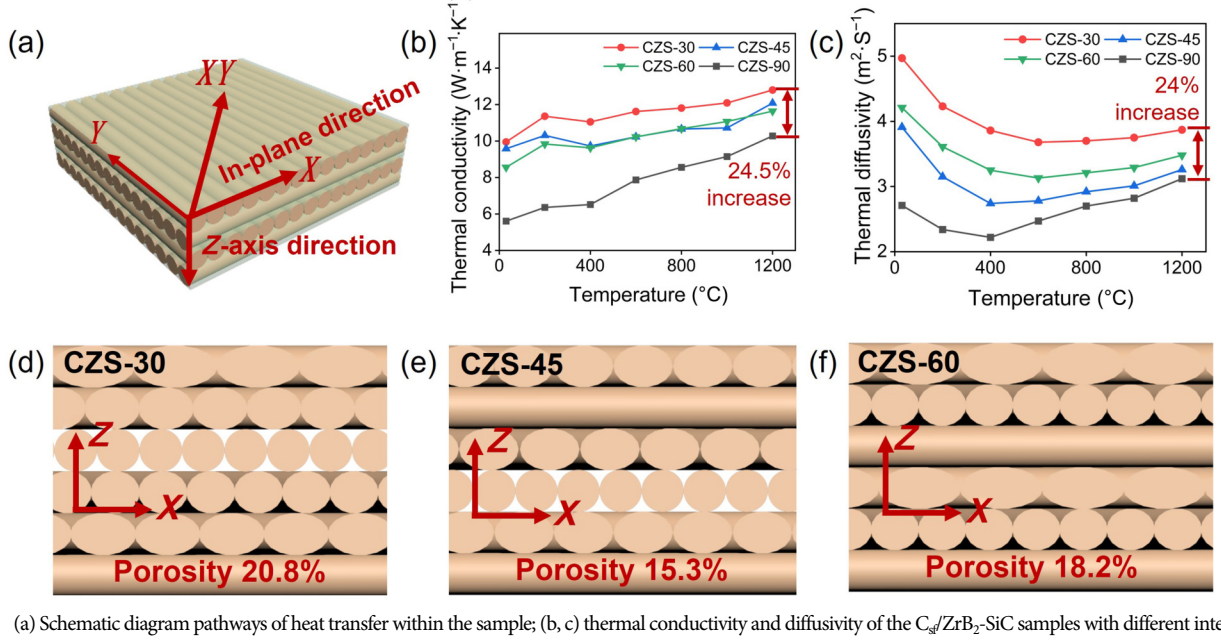

Fig. 6 (a) Schematic diagram pathways of heat transfer within the sample; (b, c) thermal conductivity and diffusivity of the C_{sf}/ZrB_2-SiC samples with different interlayer angles in the *Z*-axis direction; (d–f) schematic diagrams of the cross-section of three distinct Bouligand structure composites.

determined to be 20.8%, 15.30%, 18.2%, and 15.8%, respectively. It can be concluded that CZS-30 demonstrates the most uniform in-plane thermal diffusion, despite its relatively high porosity. This demonstrates that the positive influence of the Bouligand structure on thermal diffusion uniformity outweighs the negative effect of reduced thermal conductivity caused by high porosity. Cross-sectional analysis revealed that interlaminar pores underwent progressive collapse and deformation under thermal loading. Smaller interlayer angles (e.g., 30°) amplified this effect, promoting preferential fiber alignment along the *Z*-direction. This microstructural rearrangement facilitated phonon transport pathways, thereby elevating thermal diffusivity and conductivity. This is consistent with reported Bouligand-structured ceramics exhibiting anisotropic thermal regulation.

Furthermore, the in-plane thermal conductivity and diffusivity of the samples were determined and are summarized in Fig. 7. The introduction of the Bouligand structure does not improve the in-plane thermal conductivity or diffusivity of the composite.

To further investigate the thermal transport mechanisms in Bouligand-structured composites, we conducted multiscale modeling integrated with mathematical analysis. The in-plane thermal conductivity measurements required relatively thin samples, whereas computational models employed six-layer stacks to ensure statistical reliability. In the CZS-30 model, six layers precisely constituted one helical period (Fig. 8(a)), enabling complete phonon pathway analysis. In the CZS-45 model, the six-layer stack introduced one additional 0° and 45° layer, creating interfacial phonon scattering sites. In the CZS-60 model, two layers per orientation angle (180° rotation) facilitated comparative analysis of orthogonal fiber effects. For the CZS-90 model, symmetric stacking of three 0° and three 90° plies served as a baseline for cross-ply behavior.

All models maintained identical compositional profiles and fiber bundle thermal properties. This ensures that under uniform thermal loading, each fiber bundle exhibited equivalent thermal diffusion distances. This design enables quantitative comparison of heat flux distortion induced solely by interlayer rotation angles, revealing how Bouligand architectures modulate thermal anisotropy through helical phonon transport pathways. The thermal diffusivity is subject to a considerable impact from the

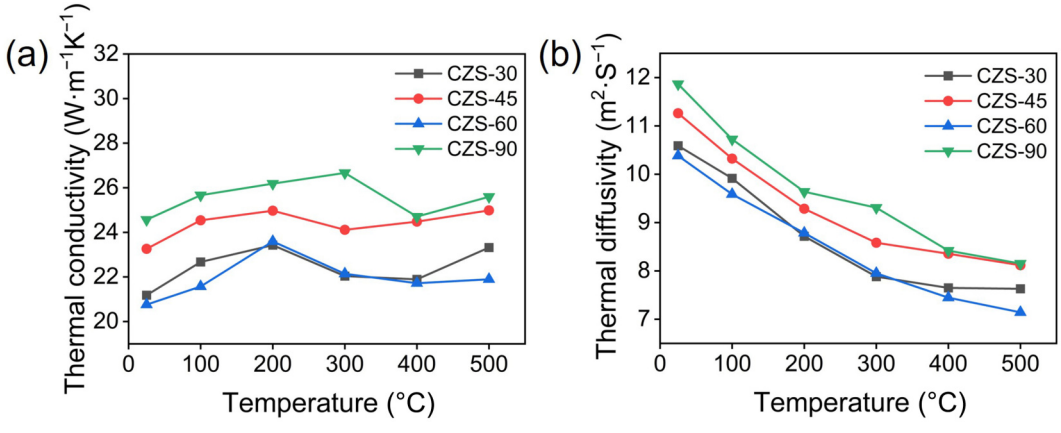

Fig. 7 (a) Thermal conductivity and (b) diffusivity of the C_{sf}/ZrB_2-SiC samples with different interlayer angles in the in-plane direction.

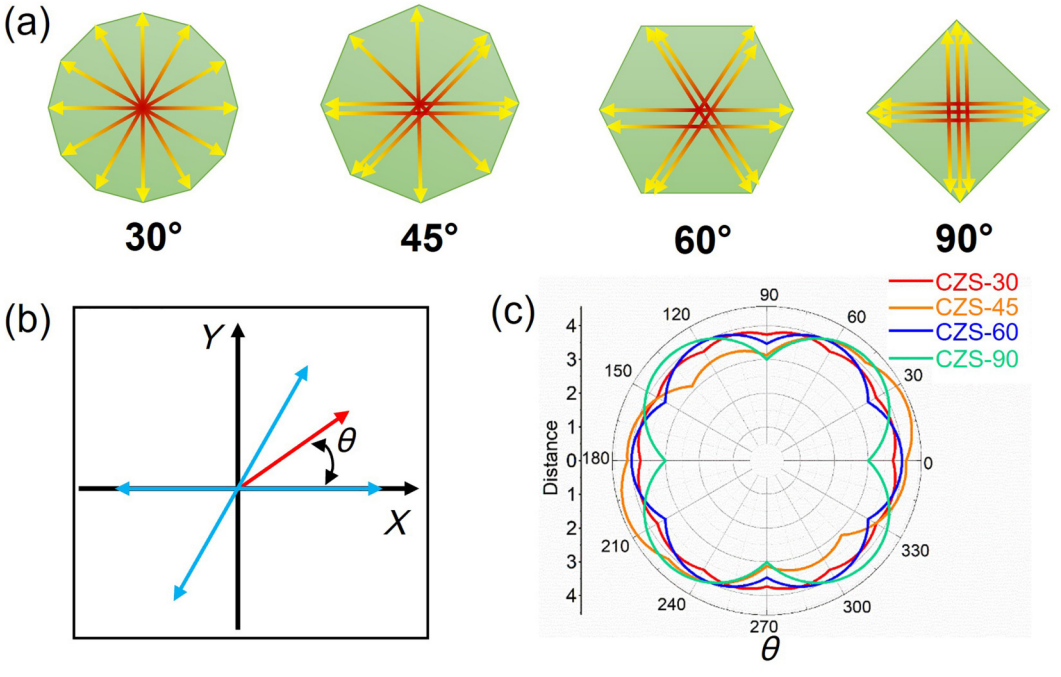

Fig. 8 (a) Thermal diffusion models for the C_{sf}/ZrB_2-SiC composites with different interlayer angles; (b) methodology for constructing the thermal diffusion distance function; (c) polar diagram of the thermal diffusion distance.

清華大学出版社 Tsinghua University Press | SciOpen

fiber/matrix interfacial thermal resistance (Kapitza effect), along with the effects of SiC phase fraction, porosity and temperature-dependent phonon scattering. However, the four samples share comparable composition and porosity levels but exhibit distinct structural characteristics. This work primarily aims to elucidate the underlying mechanism by which the Bouligand structure influences thermal diffusion in the composite. Accordingly, a simplification of the model was implemented.

The calculations were simplified by normalizing the thermal diffusion distance of the fiber bundles to 1 under identical thermal loading. For each layer, the component of this thermal diffusion distance along the θ-direction (with θ as the polar axis, Fig. 8(b)) was evaluated, yielding the following functional form (Eq. (2)):

$$\rho = \sum_{i=1}^{6} |\cos(\theta - (i-1)\times\phi)|, \quad \phi = 30^\circ, 45^\circ, 60^\circ, 90^\circ \quad (2)$$

where ϕ is the interlayer angle, ρ is the simplified thermal diffusion distance, and $|\cos(\theta - (i-1)\times\phi)|$ denotes the component of the thermal diffusion distance in the θ-direction for the ith layer. Figure 8(c) presents the polar diagram distribution of thermal diffusion distances as a function of θ, revealing distinct anisotropic patterns across samples. For CZS-90, diffusion distances along 0°/90° fiber orientations (due to preferential phonon scattering at orthogonal interfaces) are minimal, contrasting with maxima at 45°/135° (attributed to reduced interfacial thermal resistance in diagonal directions). For CZS-60, peak distances occur at 0°, 60°, and 120°, aligning with helical periodicity-induced phonon focusing effects. For CZS-45, a singular maximum at ~20° suggests localized heat channeling through intermediate-angle layers. For CZS-30, near-uniform distances are present across all orientations, demonstrating isotropic thermal transport. This is a consequence of the optimized interlayer angle suppressing phonon-boundary scattering.

Based on the above analysis, the C_{sf}/ZrB_2-SiC composite with 30° Bouligand architecture achieves synergistic enhancement: mechanical robustness via crack deflection coupled with thermal uniformity through homogenized diffusion pathways - critical for multifunctional composite design.

Figure 9(a) shows the macroscopic morphology of the Bouligand structure composites following 300 s of ablation testing at 6 MW/m² heat flux. The samples retain a smooth surface and no ablation pits after being exposed to ultrahigh temperature plasma ablation above 2000 °C (Fig. 9(b)). Moreover, all Bouligand structure composites exhibited a low linear ablation rate, which was maintained in the range of 0.13 to 0.25 μm·s^{-1}. These results confirm that the Bouligand structure composites exhibit excellent ablation resistance, making them suitable for ultrahigh temperature structural protection. Furthermore, under identical heat flux testing conditions, CZS-30 exhibited the lowest surface temperature. This result indicates that the 30° Bouligand structure enhances in-plane thermal diffusion uniformity, confirming the reliability of the thermal simulation.

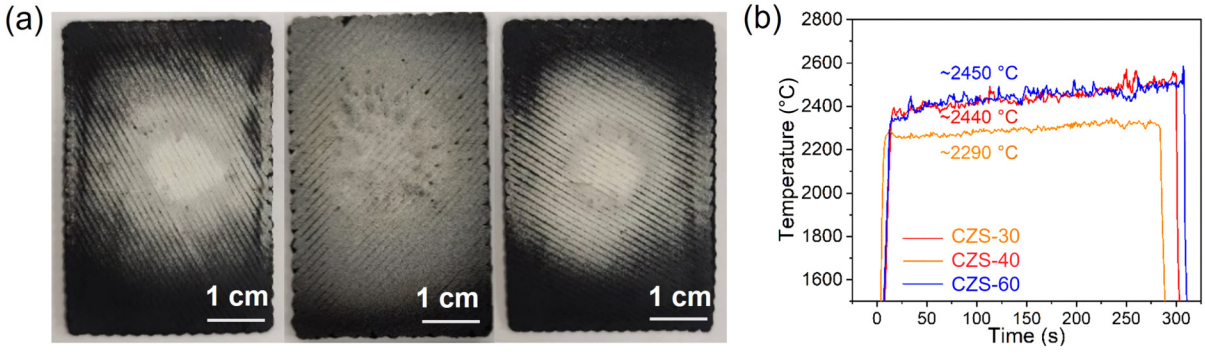

Fig. 9 (a) Macroscopic morphology of the Bouligand structure composites after 6 MW·m^{-2} ablation testing, (b) temperature–time curve of the Bouligand structure composites.

4 Conclusions

The key innovation of this work is the successful introduction of the Bouligand structure into short fiber reinforced ceramic matrix composites via 3D printing. The Bouligand structure was optimized through a combination of experiments and simulations, achieving synergistic optimization of the mechanical and thermal properties. This design addresses the key limitation of poor mechanical properties in conventional short fiber reinforced ceramic matrix composites. Simultaneously, we targeted the core issue of surface temperature during ablation by improving thermal diffusion homogeneity, resulting in a successfully lowered surface temperature. Multiscale characterization and simulation results show that the 30° Bouligand structure achieves synergistic optimization between mechanical robustness and in-plane thermal diffusion uniformity. Finite element simulations reveal that the 30° interlayer design (CZS-30) maximizes the crack deflection efficiency. It presents the longest ultimate crack path (0.2915 mm) among all samples, facilitated by hierarchical fiber bridging and pull-out mechanisms. As a result, 42% and 35% enhancements in flexural strength and fracture toughness were achieved, respectively, compared to conventional CZS-90 composites. Furthermore, the 30° structure simultaneously enhances the *Z*-axis thermal conductivity (24.5% compared to CZS-90) through aligned phonon transport pathways and in-plane diffusion uniformity by leveraging the high radial conductivity of short fibers. This dual-phase thermal regulation can effectively mitigate surface temperature gradients under extreme service conditions, which is a critical advantage for thermal protection systems. The outstanding performance synergy stems from small-angle rotation and fiber-matrix synergy. It promotes multidirectional crack deflection while minimizing interfacial phonon scattering. This work establishes a paradigm for designing next-generation C_{sf}/UHTCMCs, where Bouligand angle engineering concurrently addresses structural integrity and thermal management challenges.

Acknowledgements

The financial support from the National Natural Science Foundation of China (Nos. 52472114, 52332003, 52402135, and

52502084), Program of Shanghai Academic/Technology Research Leader (No. 23XD1424300), Science and Technology Commission of Shanghai Municipality (No. 23ZR1472100), Young Elite Scientist Sponsorship Progress by CAST (No. YESS20240518) and Postdoctoral Fellowship Program (Grade B) of China Postdoctoral Science Foundation (No. GZB20240786) is greatly acknowledged.

Availability of data and materials

The data that support the findings of this study are available from the corresponding author upon reasonable request.

Competing interests

The authors have no competing interests to declare that are relevant to the content of this article. The author Dewei Ni is the Editorial Committee member of this journal.

Electronic Supplementary Material

Supplementary material is available in the online version of this article at https://doi.org/10.26599/JAC.2025.9221232.

References

[1] Zhang XH, Wang YM, Cheng Y, *et al.* Research progress on ultra-high temperature ceramic composites. *J Inorg Mater* 2024, **39**: 571.

[2] Jiang TX, Wen QB, Lu L, *et al.* (Ti,Zr,Hf,Ta)CN/SiCN: A new ultrahigh-temperature ceramic nanocomposite with excellent mechanical properties and ablation resistance. *J Adv Ceram* 2025, **14**: 9221104.

[3] Ye ZM, Zeng Y, Xiong X, *et al.* Revealing the solid-state reaction process among multiphase multicomponent ceramic during ablation. *Adv Powder Mater* 2024, **3**: 100189.

[4] Lyu Y, Han ZH, Cheng Y, *et al.* Ablation behavior of 3D PyC-C_f/SiHfBOC Composites under an oxyacetylene torch environment above 2000 °C. *Ceram Int* 2024, **50**: 14011–14019.

[5] Li JC, Lu FY, Li T, *et al.* Superior synergistic oxidation resistance of medium-entropy carbide ceramic powders rather than multi-phase carbide ceramic powders. *J Adv Ceram* 2024, **13**: 1223–1233.

[6] Lyu Y, Han ZH, Zhao GD, *et al.* Efficient fabrication of light C_f/SiHfBOC composites with excellent thermal shock resistance and ultra-high-temperature ablation up to 1800 °C. *J Adv Ceram* 2023, **12**: 2062–2074.

[7] Huang FL, Wang HL, Fang C, *et al.* Improved damage tolerance and oxidation resistance of $(Ti_{0.2}Zr_{0.2}Hf_{0.2}Nb_{0.2}Ta_{0.2})B_2$–SiC by introducing chopped carbon fibers. *J Adv Ceram* 2024, **13**: 101–112.

[8] Zhao T, Liu JX, Xu YX, *et al.* The effect of SiC on the laser ablation resistance of high-entropy diboride ceramics. *Adv Ceram* 2024, **45**: 417–433. (in Chinese)

[9] Fang C, Dong S, Zhang XH, *et al.* Breaking the 3000 °C melting temperature barrier of oxide ceramics. *J Adv Ceram* 2025, **14**: 9221193.

[10] Lyu Y, Hao JC, Cheng Y, *et al.* Ultrahigh temperature ablation resistant HfB_2-SiC composites: From liquid SiHfCB precursor synthesis to light weight bulk preparation and characterization. *J Mater Sci Technol* 2025, **212**: 1–16.

[11] Ji PY, Lei XY, Fu QG, *et al.* Effect of fiber type on the ablation resistance of sharp leading-edge C/C-ZrB_2-SiC composites: Mesophase pitch carbon fibers vs. *PAN-based fibers. Compos Commun* 2025, **59**: 102582.

[12] Hou JQ, Zhang JP, Chen RC, *et al.* An area-tailored (Hf,Ta)B_2-SiC coating for ultra-high thermal protection: Design and evolution of microstructure. *Corros Sci* 2025, **257**: 113353.

[13] Wang RN, He CX, Zhang JP, *et al.* 2.5D woven *vs.* 2.5D needled Preforms: Influencing microstructure evolution, mechanical properties and ablation behavior in C/C–ZrC–SiC based composites. *Compos Part B Eng* 2025, **307**: 112908.

[14] Lu J, Ni DW, Liao CJ, *et al.* Fabrication and microstructure evolution of Csf/ZrB_2-SiC composites via direct ink writing and reactive melt infiltration. *J Adv Ceram* 2021, **10**: 1371–1380.

[15] An YM, Wan K, Yang Y, *et al.* Fabrication method and mechanical properties of biomimetic C_f/ZrB_2-SiC ceramic composites with bouligand structures. *J Eur Ceram Soc* 2023, **43**: 283–290.

[16] Gao Q, Hu P, Xun LC, *et al.* A scalable method allows for the rapid fabrication of C/SiC composites with excellent mechanical properties and ablation resistance. *J Adv Ceram* 2025, **14**: 9221162.

[17] Shi Y, Hausherr JM, Hoffmann H, *et al.* Inspection of geometry influence and fiber orientation to characteristic value for short fiber reinforced ceramic matrix composite under bending load. *J Eur Ceram Soc* 2017, **37**: 1291–1303.

[18] Peng Z, Ma QS, Cui YJ, *et al.* Tailored C_{sf}/$HfC_{0.76}N_{0.24}$ composites for superior ablation resistance at 3000 °C. *Adv Powder Mater* 2025, **4**: 100281.

[19] Xu YX, Yu L, Zhao T, *et al.* Composition design of oxidation resistant non-equimolar high-entropy ceramic materials: An example of (Zr–Hf–Ta–Ti)B_2 ultra-high temperature ceramics. *J Adv Ceram* 2024, **13**: 2087–2100.

[20] Wang WQ, Li ZC, Gao X, *et al.* Material extrusion 3D printing of large-scale SiC honeycomb metastructure for ultra-broadband and high temperature electromagnetic wave absorption. *Addit Manuf* 2024, **85**: 104158.

[21] Zhao XN, Zhu ZP. A facile strategy for constructing biomimetic continuous fiber reinforced biocomposites with spatial Bouligand structure. *Compos Commun* 2025, **56**: 102351.

[22] Guan LZ, Peng WX, Wen RNJ, *et al.* Izod impact resistance of 3D printed discontinuous fibrous composites with Bouligand structure. *NPG Asia Mater* 2023, **15**: 60.

[23] Chen SM, Wu KJ, Gao HL, *et al.* Biomimetic discontinuous Bouligand structural design enables high-performance nanocomposites. *Matter* 2022, **5**: 1563–1577.

[24] Wang HX, Cheng LD, Yu JY, *et al.* Biomimetic Bouligand chiral fibers array enables strong and superelastic ceramic aerogels. *Nat Commun* 2024, **15**: 336.

[25] Zimmermann EA, Gludovatz B, Schaible E, *et al.* Mechanical adaptability of the Bouligand-type structure in natural dermal armour. *Nat Commun* 2013, **4**: 2634.

[26] Zhang RK, Wang SY, Zheng LY, *et al.* Bamboo-inspired fibrous monolithic high-entropy carbide ceramics with enhanced toughness and thermal insulation performance. *J Adv Ceram* 2025, **14**: 9221190.

[27] Wang H, Liu JR, Wu ZY, *et al.* Bioinspired strong and tough layered bulk composites via mycelial interface anchoring strategy. *Adv Sci* 2025, **12**: 2413226.

[28] Ling SJ, Kaplan DL, Buehler MJ. Nanofibrils in nature and materials engineering. *Nat Rev Mater* 2018, **3**: 18016.

[29] Chen JY, Su RY, Zhang XQ, *et al.* 3D printed leaf-vein-like Al_2O_3/EP biohybrid structures with enhanced thermal conductivity. *ACS Appl Mater Interfaces* 2024, **16**: 56191–56198.

[30] Chen SM, Wang GZ, Hou YZ, *et al.* Hierarchical and reconfigurable interfibrous interface of bioinspired Bouligand structure enabled by moderate orderliness. *Sci Adv* 2024, **10**: eadl1884.

[31] Lu L, Wang SB, Jiang TX, *et al.* Nature-inspired (Ti,Zr,Hf)C/SiC micro–nano composites with enhanced ablation resistance through a Gobi desert-like protective oxide layer. *J Adv Ceram* 2025, **14**: 9221151.

[32] Hu Y, Ni DW, Chen BW, *et al.* Ultra-light gradient C_f/(CrZrHfNbTa)C-SiC composite all-in-one strategy enables efficient thermal insulation, EMI shielding and ablation resistance. *J Mater Sci Technol* 2025, **235**: 302–312.